

Categorization of two-loop Feynman diagrams in the $\mathcal{O}(\alpha^2)$ correction to $e^+e^- \rightarrow ZH$ *

Zhao Li ^{1,2,3} Yefan Wang^{1,2} Quan-feng Wu ^{1,2}

¹ Institute of High Energy Physics, Chinese Academy of Sciences, Beijing 100049, China

² School of Physics Sciences, University of Chinese Academy of Sciences, Beijing 100039, China

³ Center of High Energy Physics, Peking University, Beijing 100871, China

Abstract: The $e^+e^- \rightarrow ZH$ process is the dominant process for the Higgs boson production at the future Higgs factory. In order to match the analysis on the Higgs properties with the highly precise experiment data, it will be crucial to include the theoretical prediction to the full next-to-next-to-leading order electroweak effect in the production rate $\sigma(e^+e^- \rightarrow ZH)$. In this inspiring work, we categorize the two-loop Feynman diagrams of the $\mathcal{O}(\alpha^2)$ correction to $e^+e^- \rightarrow ZH$ into 6 categories according to the relevant topological structures. Although 25377 diagrams contribute to the $\mathcal{O}(\alpha^2)$ correction in total, the number of the most challenging diagrams with seven denominators is 2250, which contain only 312 non-planar diagrams with 155 independent types. This categorization could be a valuable reference for the complete calculation in the future.

Key words: Categorization, Higgsstrahlung, $\mathcal{O}(\alpha^2)$ correction

1 Introduction

The discovery of the Higgs boson in 2012 at the Large Hadron Collider (LHC) [1, 2] has opened a new era in the particle physics. In particular, the Higgs boson is regarded as the key to solve some challenging problems such as the problem of hierarchy, the origin of the neutrino mass and the dark matter problem. Consequently the precise measurements of the Higgs boson properties have become top priorities of both experimental and theoretical particle physics.

Although the LHC can produce a lot of Higgs bosons, the enormously complicated QCD backgrounds make the sufficiently precise measurements hard to achieve. To precisely measure the properties of the Higgs boson, the next generation e^+e^- colliders have been proposed as the Higgs factories aiming at much higher accuracy of measurements. Compared to the LHC, the e^+e^- colliders will have cleaner experiment conditions and higher luminosity. The candidates of the next generation e^+e^- colliders include Circular Electron Positron Collider (CEPC) [3, 4], International Linear Collider (ILC) [5–7] and Future Circular Collider (FCC-ee) [8–10]. All of them are designed to operate at the center-of-mass energy $\sqrt{s} \sim 240\text{--}250$ GeV. In this energy range, the processes to produce Higgs bosons are $e^+e^- \rightarrow ZH$ (Higgsstrahlung), $e^+e^- \rightarrow \nu_e \bar{\nu}_e H$ (W fusion) and $e^+e^- \rightarrow e^+e^- H$ (Z fusion). The dominant Higgs production process is the Higgsstrahlung. And the recoil mass method can be ap-

plied to identify the Higgs boson candidates [3, 9, 11–13]. Then the Higgs boson production can be disentangled in a model-independent way.

At the CEPC, over one million Higgs bosons can be produced in total with the expected integrated luminosity of 5.6 ab^{-1} [14]. With these sizable events, many important properties of the Higgs boson can be measured in a high accuracy. For instance, the cross section $\sigma(e^+e^- \rightarrow ZH)$ can be measured to the extremely high precision 0.51% [14]. Since the Higgs boson candidate events can be identified by recoil mass method, the measurements of HZZ coupling mainly depend on the precise measurement of $\sigma(e^+e^- \rightarrow ZH)$. Consequently, it is expected that the experiment error in the HZZ coupling can be 0.25% at the CEPC, which is much better than at the HL-LHC [15, 16].

Furthermore, such precise measurements give the CEPC unprecedented reach into the new physics scenarios which are difficult to probe at the LHC [17]. In the natural supersymmetry (SUSY), typically dominant effect on Higgs precision from colored top partners may have blind spots [18, 19]. The blind spots can be filled in by the measurement of $\sigma(e^+e^- \rightarrow ZH)$, which is sensitive to loop-level corrections to the tree-level HZZ coupling [17]. When the $\delta\sigma_{ZH}$ approaches to 0.2%, the further constraints for $m_{\tilde{t}_1}$ and $m_{\tilde{t}_2}$ can be observed [20]. And the HZZ coupling plays an important role in the study of Electroweak Phase Transition (EWPT). In the real scalar singlet model [21–23], the first order phase tran-

* This work was supported by the National Natural Science Foundation of China under Grant No. 11675185 and 12075251.

1) E-mail: zhaoli@ihep.ac.cn

2) E-mail: wangyefan@ihep.ac.cn

3) E-mail: wuquanfeng@ihep.ac.cn

sition tends to predict a large suppression of the HZZ coupling ranging from 1% to as much as 30% [24]. With the expected sensitivity of δg_{HZZ} at the CEPC, the models with a strongly first order phase transition can be tested.

Beside the improvement on the experiment accuracy, the higher precision theoretical prediction for $\sigma(e^+e^- \rightarrow ZH)$ is also demanded to match the precision of experiment measurements. The next-to-leading-order (NLO) electroweak (EW) corrections to $\sigma(e^+e^- \rightarrow ZH)$ have been investigated two decades ago [25–27]. And the next-to-next-to-leading-order (NNLO) EW-QCD corrections have also been calculated in recent years [28–30]. The results show that the NNLO EW-QCD corrections increase the cross section more than one percent, which is larger than the expected experiment accuracies of the CEPC. On the other hand, it indicates the NNLO EW corrections can be significant. And it is necessary to emphasize that the corrections depend crucially on the renormalization schemes. In $\alpha(0)$ scheme, the NNLO EW-QCD corrections are about 1.1% of the leading-order (LO) cross section. But in G_μ scheme, the NNLO EW-QCD corrections only amount to 0.3% of LO cross section [29]. And the sensitivity to the different scheme is reduced by NNLO EW-QCD corrections compared to NLO EW corrections. Consequently the EW-QCD σ_{NNLO} ranges from 231 fb to 233 fb.

Hence, the missing two-loop corrections to $\sigma(e^+e^- \rightarrow ZH)$ can still lead to an intrinsic uncertainty of $\mathcal{O}(1\%)$ [31], which is still larger than the experiment accuracy. Since $\sigma(e^+e^- \rightarrow ZH)$ is proportional to the square of the HZZ coupling, the theoretical uncertainties also have a significant impact on the extracting of HZZ coupling. Then the accuracy of HZZ coupling (0.25%) in the CEPC may not be achieved due to the large theoretical uncertainties. Recently, some interesting calculations toward NNLO EW correction have been made such as [32]. We believe that if the full NNLO EW corrections to $\sigma(e^+e^- \rightarrow ZH)$ can be calculated, the scheme dependence can be further reduced to stabilize the theoretical prediction.

Due to the complicity of EW interaction, there are more than 20 thousand Feynman diagrams contribute to the $\mathcal{O}(\alpha^2)$ correction of $e^+e^- \rightarrow ZH$. The complete calculations of these Feynman diagrams are huge projects. Therefore, in this paper we focus on the categorization of these Feynman diagrams. This categorization could be helpful for the future calculations and analyses. In the next section we will categorize the Feynman diagrams into six categories and dozens of subcategories. Then the conclusion is made.

2 Categorization

In the Feynman gauge, we obtain 25377 diagrams contributing to the $\mathcal{O}(\alpha^2)$ corrections of $e^+e^- \rightarrow ZH$ by using FEAMGEN*. Here we have chosen the Yukawa couplings of light fermions (all fermions except the top quark) as zero. FEYNARTS [34] is used to check the correctness to this procedure.

To categorize these diagrams, first we put the diagrams which can be factorized into two one-loop diagrams to the category \mathcal{C}_1 . Then according to the number of denominators in each diagram, we categorize the remaining non-factorizable two-loop diagrams into five categories $\mathcal{C}_2, \dots, \mathcal{C}_6$. Furthermore, according to the topologies of loop structures \mathcal{C}_i can be categorized into several subcategories $\{\mathcal{C}_{i,j}\}$. Since the light quarks are regarded as massless except the top quark, we use $\mathcal{C}_{i,j,a}$ ($\mathcal{C}_{i,j,b}$) to denote the diagrams without (with) the top quark.[†] Since some amplitudes can be obtained by replacing coupling factors or masses from other diagrams, $\mathcal{C}_{i,j}$ can be reduced to subset $\mathcal{C}_{i,j}^{\text{ind}}$ which only includes the "independent" diagrams. Due to the color structure and conservation laws, 153 diagrams in total have zero amplitudes.

In this paper we use the Nickel index [35–37] to describe the topologies of loop structures. For reader's convenience we briefly explain the Nickel notation and Nickel index. Nickel notation is a labelling algorithm to describe connected undirected graphs with "simple" edges and vertices such as the topological structures of the Feynman diagrams. First, one should consider a connected graph with n vertices and label these n vertices by the integers 0 through $n-1$ at random. Therefore, the sequence can be constructed according to [35, 36]:

$$\begin{aligned} & \text{vertices connected to vertex } 0 \mid \\ & \text{vertices connected to } 1 \text{ excluding } 0 \mid \dots \mid \\ & \text{vertices connected to vertex } i \text{ excluding } 0 \text{ through } i-1 \mid \\ & \dots \mid. \end{aligned} \tag{1}$$

For instance, Fig.1(a) can be represented by 12|223|3|. Otherwise, we can use the label "e"s to describe the external lines in the diagrams. Also, the Nickel notation of Fig.1(b) is ee11|ee|. With different labeling strategy, one diagram can be represented as some different Nickel notations, which describe the same diagram up to a topological homeomorphism. For simplicity, the Nickel index algorithm can be used to find the "minimal" Nickel notation, which is called Nickel index. Consequently, the diagram and its Nickel index are in one-to-one correspondence. For instance, the Nickel index of Fig.1(a) is 1123|23|||. The package GRAPHSTATE [35] is the useful tool for constructing the Nickel index. The detail of the

*The Julia package (<https://github.com/zhaoli-IHEP/FeAmGen.jl>) interfaced to QGRAF [33].

[†]The complete PDF files of all subcategories can be downloaded in https://github.com/zhaoli-IHEP/eeHZ_nnloEW_diagrams.

Nickel index algorithm can be found in Ref. [35].

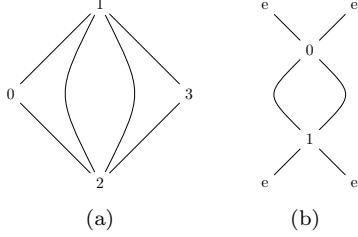


Fig. 1: Nickel notation and Nickel index

In this paper, the topological structures of the diagrams with one vertex connecting to one or two external legs are regarded as equivalent. For instance, the topological structures of two diagrams in Fig.2 can be regarded as equivalent.

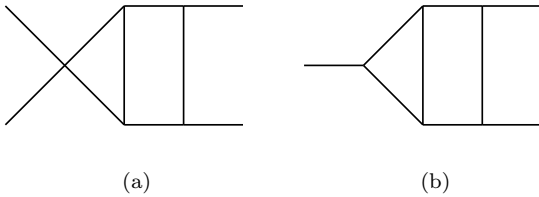


Fig. 2: The example of equivalent topological structures

2.1 Category \mathcal{C}_1

The category \mathcal{C}_1 includes 7908 Feynman diagrams that can be factorized into two one-loop diagrams. Therefore, the calculations of diagrams in \mathcal{C}_1 can be regarded as the one-loop level calculations. According to the topologies of loop structures in \mathcal{C}_1 , they are categorized into 3 subcategories.

The subcategory $\mathcal{C}_{1,1}$ includes 2117 diagrams which contain at least one one-loop vacuum bubble diagram. Furthermore $\mathcal{C}_{1,1,a}$ includes 2055 diagrams and $\mathcal{C}_{1,1,b}$ includes 62 diagrams. In $\mathcal{C}_{1,1,b}$, there are 14 diagrams whose amplitudes equal to zero. $\mathcal{C}_{1,1,a}^{ind}$ has 449 independent diagrams and $\mathcal{C}_{1,1,b}^{ind}$ has 36 independent diagrams. We choose diagram #47 as the representative of $\mathcal{C}_{1,1,a}$ and diagram #4418 as the representative of $\mathcal{C}_{1,1,b}$.

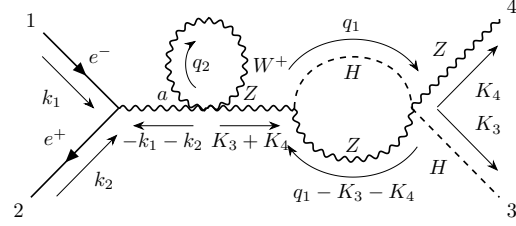


Fig. 3: Diagram #47 (representative of $\mathcal{C}_{1,1,a}$)

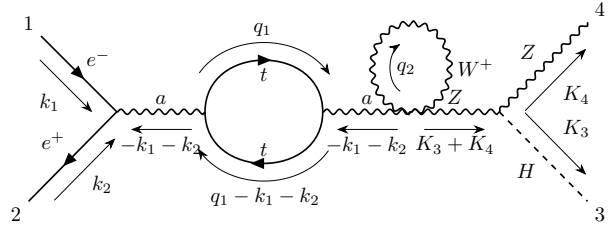


Fig. 4: Diagram #4418 (representative of $\mathcal{C}_{1,1,b}$)

The subcategory $\mathcal{C}_{1,2}$ includes 5513 diagrams that contain self-energy corrections. And the diagrams $\mathcal{C}_{1,2}$ do not contain vacuum bubble diagrams. $\mathcal{C}_{1,2,a}$ includes 4775 diagrams and $\mathcal{C}_{1,2,b}$ includes 738 diagrams. In $\mathcal{C}_{1,2,b}$ there are 131 diagrams whose amplitudes equal to zero. $\mathcal{C}_{1,2,a}^{ind}$ has 740 independent diagrams and $\mathcal{C}_{1,2,b}^{ind}$ has 278 independent diagrams. We choose diagram #36 as the representative of $\mathcal{C}_{1,2,a}$ and diagram #1035 as the representative of $\mathcal{C}_{1,2,b}$.

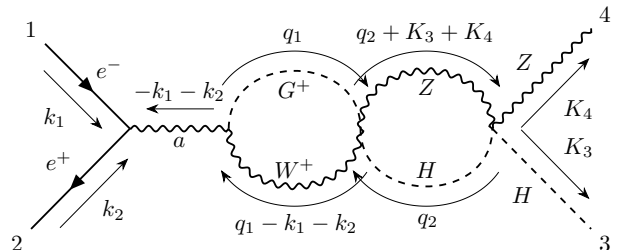


Fig. 5: Diagram #36 (representative of $\mathcal{C}_{1,2,a}$)

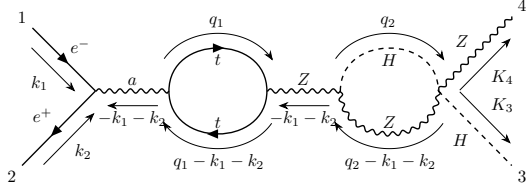


Fig. 6: Diagram #1035 (representative of $\mathcal{C}_{1,2,b}$)

The subcategory $\mathcal{C}_{1,3}$ includes 278 diagrams which contain two vertex corrections. $\mathcal{C}_{1,3,a}$ includes 260 diagrams and $\mathcal{C}_{1,3,b}$ includes 18 diagrams. $\mathcal{C}_{1,3,a}^{ind}$ has 68 independent diagrams and $\mathcal{C}_{1,3,b}^{ind}$ has 14 independent diagrams. We choose diagram #6983 as the representative of $\mathcal{C}_{1,3,a}$ and diagram #23660 as the representative of $\mathcal{C}_{1,3,b}$.

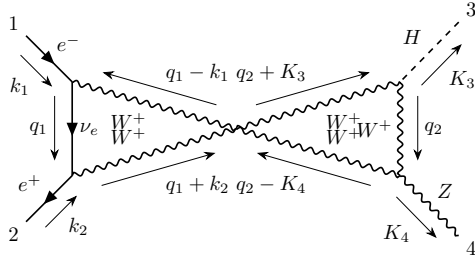


Fig. 7: Diagram #6983 (representative of $\mathcal{C}_{1,3,a}$)

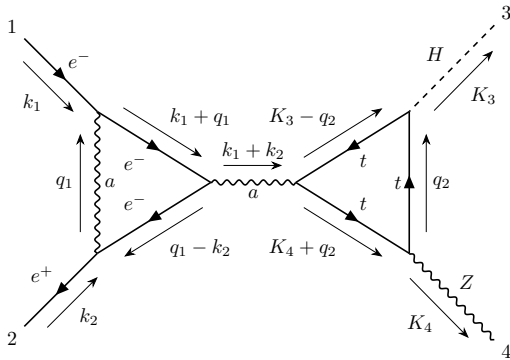


Fig. 8: Diagram #23660 (representative of $\mathcal{C}_{1,3,b}$)

2.2 Category \mathcal{C}_2

The category \mathcal{C}_2 includes non-factorizable two-loop Feynman diagrams with three denominators. We found that all diagrams in \mathcal{C}_2 are two-loop self-energy diagrams. \mathcal{C}_2 includes 18 diagrams, none of which contains top

quark. \mathcal{C}_2^{ind} has 8 independent diagrams. We choose diagram #519 as the representative of \mathcal{C}_2 .

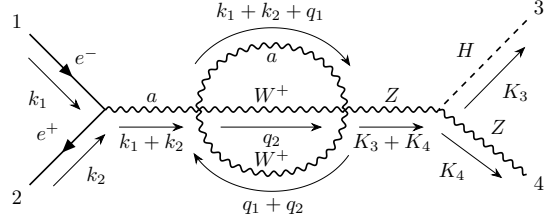


Fig. 9: Diagram #519 (representative of \mathcal{C}_2)

2.3 Category \mathcal{C}_3

The category \mathcal{C}_3 includes 593 non-factorizable two-loop Feynman diagrams with four denominators. According to the topologies of loop structures in \mathcal{C}_3 , we categorize them into 3 subcategories.

The subcategory $\mathcal{C}_{3,1}$ includes 142 diagrams which can be separated into the tree-level diagrams and the two-loop vacuum bubble diagrams. The topology of their loop structures can be noted as 112|2|| in Nickel index. The calculation of the two-loop vacuum bubble diagram has been well studied [38]. $\mathcal{C}_{3,1}^{ind}$ has 51 independent diagrams. We choose diagram #3961 as the representative of $\mathcal{C}_{3,1}$.

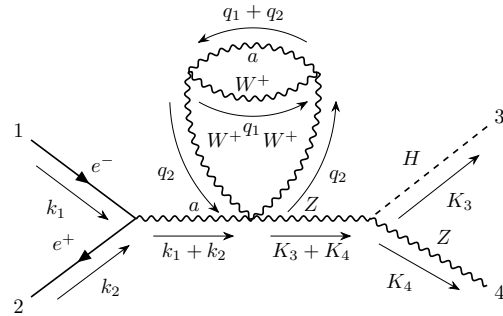


Fig. 10: Diagram #3961 (representative of $\mathcal{C}_{3,1}$)

The subcategory $\mathcal{C}_{3,2}$ includes 337 two-loop self-energy diagrams, none of which contains top quark. $\mathcal{C}_{3,2}^{ind}$ has 93 independent diagrams. We choose diagram #1 as the representative of $\mathcal{C}_{3,2}$.

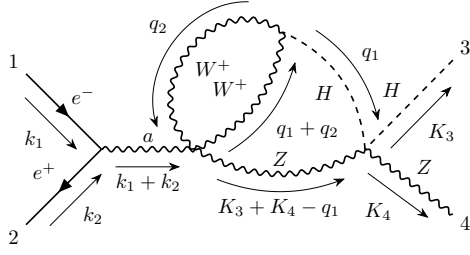


Fig. 11: Diagram #1 (representative of $\mathcal{C}_{3,2}$)

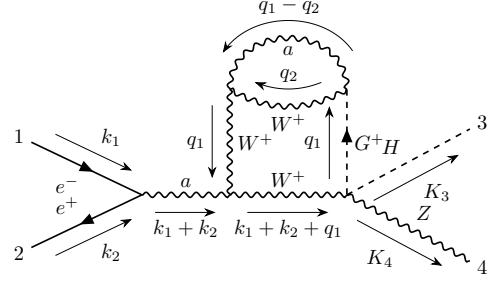


Fig. 13: Diagram #603 (representative of $\mathcal{C}_{4,1,a}$)

The subcategory $\mathcal{C}_{3,3}$ includes 114 two-loop vertex correction diagrams, none of which contains top quark. The topology of their loop structures can be noted as $e112|e2|e|$ in Nickel index. And the denominators of diagrams in $\mathcal{C}_{3,3}$ only depend on two external momenta. $\mathcal{C}_{3,3}^{ind}$ has 24 independent diagrams. We choose diagram #191 as the representative of $\mathcal{C}_{3,3}$.

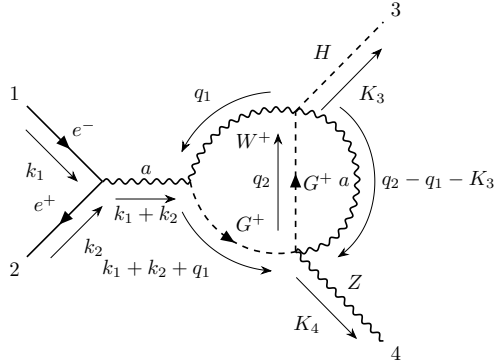


Fig. 12: Diagram #191 (representative of $\mathcal{C}_{3,3}$)

2.4 Category \mathcal{C}_4

The category \mathcal{C}_4 includes 4773 non-factorizable two-loop Feynman diagrams with five denominators. According to the topologies of loop structures in \mathcal{C}_4 , we categorize them into 3 subcategories.

The subcategory $\mathcal{C}_{4,1}$ includes 3266 two-loop self-energy diagrams, some of which contain top quark. $\mathcal{C}_{4,1,a}$ includes 2565 diagrams and $\mathcal{C}_{4,1,b}$ includes 701 diagrams. $\mathcal{C}_{4,1,a}^{ind}$ has 753 independent diagrams and $\mathcal{C}_{4,1,b}^{ind}$ has 249 independent diagrams. We choose diagram #603 as the representative of $\mathcal{C}_{4,1,a}$ and diagram #611 as the representative of $\mathcal{C}_{4,1,b}$.

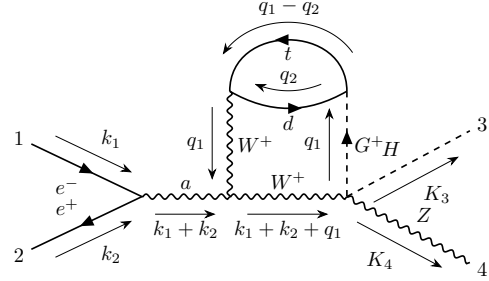


Fig. 14: Diagram #611 (representative of $\mathcal{C}_{4,1,b}$)

The subcategory $\mathcal{C}_{4,2}$ includes 637 two-loop vertex correction diagrams, none of which contains top quark. The topology of their loop structures can be noted as $e12|e23|3|e|$ in Nickel index. And the denominators of diagrams in $\mathcal{C}_{4,2}$ only depend on two external momenta. $\mathcal{C}_{4,2}^{ind}$ has 140 independent diagrams. We choose diagram #2676 as the representative of $\mathcal{C}_{4,2}$.

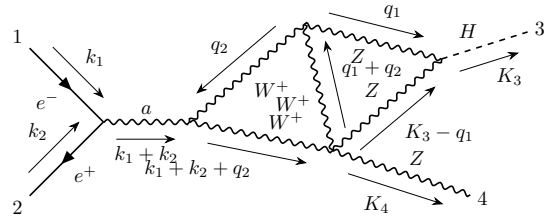


Fig. 15: Diagram #2676 (representative of $\mathcal{C}_{4,2}$)

The subcategory $\mathcal{C}_{4,3}$ includes 870 two-loop vertex correction diagrams, none of which contains top quark. The topology of their loop structures can be noted as $e112|3|e3|e|$ in Nickel index. And the denominators of diagrams in $\mathcal{C}_{4,3}$ only depend on two external momenta. $\mathcal{C}_{4,3}^{ind}$ has 278 independent diagrams. We choose diagram #3063 as the representative of $\mathcal{C}_{4,3}$.

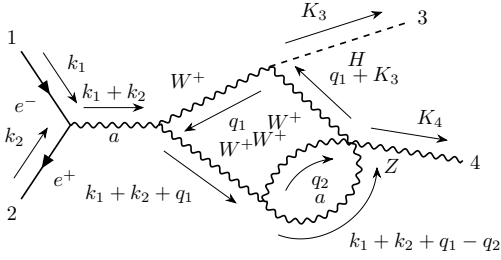


Fig. 16: Diagram #3063 (representative of $\mathcal{C}_{4,3}$)

2.5 Category \mathcal{C}_5

The category \mathcal{C}_5 includes 9835 non-factorizable two-loop Feynman diagrams with six denominators. According to the topologies of loop structures in \mathcal{C}_5 , we categorize them into six subcategories.

The subcategory $\mathcal{C}_{5,1}$ includes two-loop planar triangle diagrams. The topology of their loop structures can be noted as $\epsilon 12|e3|34|4|e|$ in Nickel index. And the denominators of diagrams in $\mathcal{C}_{5,1}$ only depend on two external momenta. $\mathcal{C}_{5,1}$ includes 4897 diagrams, some of which contain top quark. Then $\mathcal{C}_{5,1,a}$ includes 3966 diagrams and $\mathcal{C}_{5,1,b}$ includes 931 diagrams. $\mathcal{C}_{5,1,a}^{ind}$ has 1039 independent diagrams and $\mathcal{C}_{5,1,b}^{ind}$ has 397 independent diagrams. We choose diagram #1325 as the representative of $\mathcal{C}_{5,1,a}$ and diagram #16206 as the representative of $\mathcal{C}_{5,1,b}$.

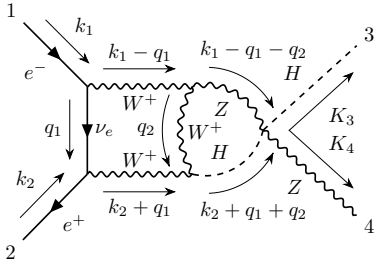


Fig. 17: Diagram #1325 (representative of $\mathcal{C}_{5,1,a}$)

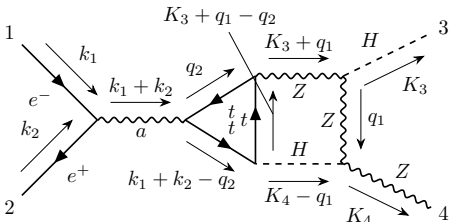


Fig. 18: Diagram #16206 (representative of $\mathcal{C}_{5,1,b}$)

The subcategory $\mathcal{C}_{5,2}$ includes 184 two-loop planar diagrams, none of which contains top quark. The topology of their loop structures can be noted as $\epsilon 12|e23|4|e4|e|$ in Nickel index. $\mathcal{C}_{5,2}^{ind}$ has 90 independent diagrams. We choose diagram #3613 as the representative of $\mathcal{C}_{5,2}$.

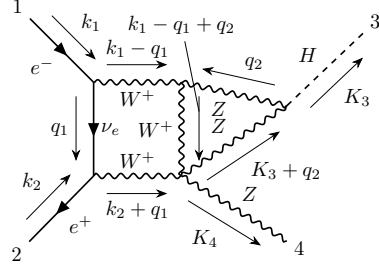


Fig. 19: Diagram #3613 (representative of $\mathcal{C}_{5,2}$)

The subcategory $\mathcal{C}_{5,3}$ includes two-loop planar diagrams. The topology of their loop structures can be noted as $\epsilon 12|e3|e4|44||$ in Nickel index. And the denominators of diagrams in $\mathcal{C}_{5,3}$ only depend on two external momenta. $\mathcal{C}_{5,3}$ includes 4067 diagrams, some of which contain top quark. $\mathcal{C}_{5,3,a}$ includes 3260 diagrams and $\mathcal{C}_{5,3,b}$ includes 807 diagrams. In $\mathcal{C}_{5,3,b}$, there are 131 diagrams whose amplitudes equal to zero. $\mathcal{C}_{5,3,a}^{ind}$ has 1077 independent diagrams and $\mathcal{C}_{5,3,b}^{ind}$ has 264 independent diagrams. We choose diagram #14794 as the representative of $\mathcal{C}_{5,3,a}$ and diagram #14812 as the representative of $\mathcal{C}_{5,3,b}$.

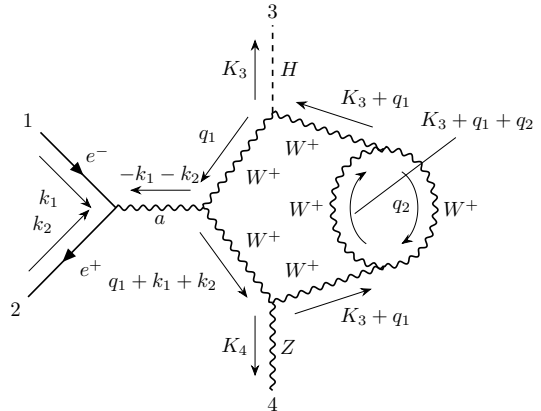


Fig. 20: Diagram #14794 (representative of $\mathcal{C}_{5,3,a}$)

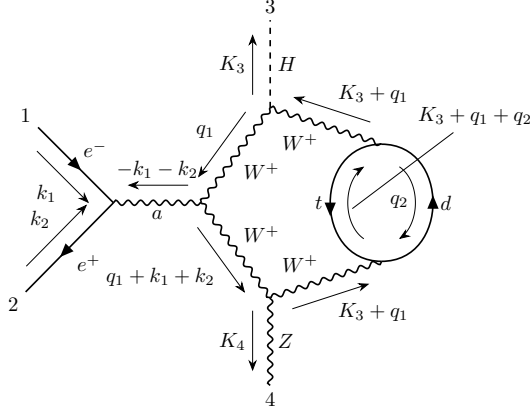


Fig. 21: Diagram #14812 (representative of $\mathcal{C}_{5,3,b}$)

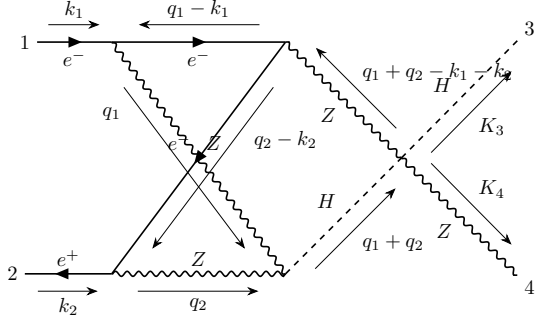


Fig. 23: Diagram #1267 (representative of $\mathcal{C}_{5,5,a}$)

The subcategory $\mathcal{C}_{5,4}$ includes two-loop planar diagrams. The topology of their loop structures can be noted as $e112|3|e4|e4|e|$ in Nickel index. $\mathcal{C}_{5,4}$ includes 116 Feynman diagrams, none of which contains top quark. $\mathcal{C}_{5,4}^{ind}$ has 70 independent diagrams. We choose diagram #3845 as a representative of $\mathcal{C}_{5,4}$.

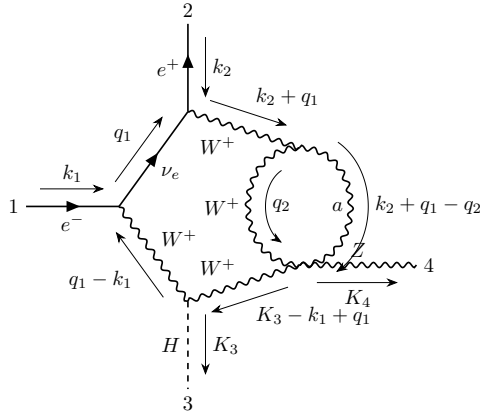


Fig. 22: Diagram #3845 (representative of $\mathcal{C}_{5,4}$)

The subcategory $\mathcal{C}_{5,5}$ includes two-loop non-planar triangle diagrams. The topology of their loop structures can be noted as $e12|34|34|e|e|$ in Nickel index. And the denominators of diagrams in $\mathcal{C}_{5,5}$ only depend on two external momenta. $\mathcal{C}_{5,5}$ includes 560 diagrams, some of which contain top quark. $\mathcal{C}_{5,5,a}$ includes 442 diagrams and $\mathcal{C}_{5,5,b}$ includes 118 diagrams. $\mathcal{C}_{5,5,a}^{ind}$ has 140 independent diagrams and $\mathcal{C}_{5,5,b}^{ind}$ has 54 independent diagrams. We choose diagram #1267 as the representative of $\mathcal{C}_{5,5,a}$ and diagram #11100 as the representative of $\mathcal{C}_{5,5,b}$.

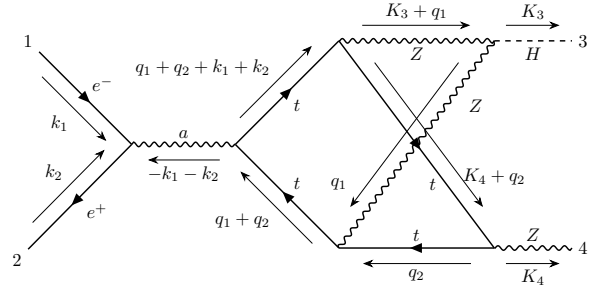


Fig. 24: Diagram #11100 (representative of $\mathcal{C}_{5,5,b}$)

The subcategory $\mathcal{C}_{5,6}$ includes two-loop non-planar diagrams. The topology of their loop structures can be noted as $e12|e34|34|e|e|$ in Nickel index. $\mathcal{C}_{5,6}$ includes 11 diagrams, none of which contains top quark. $\mathcal{C}_{5,6}^{ind}$ has 8 independent diagrams. We choose diagram #3602 as the representative of $\mathcal{C}_{5,6}$.

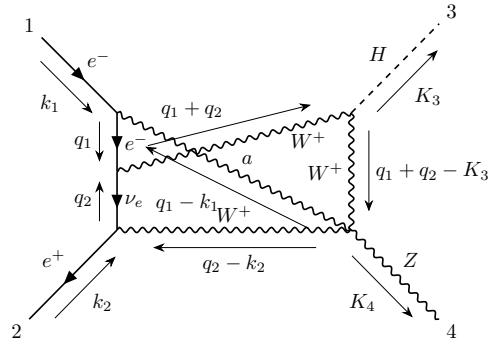


Fig. 25: Diagram #3602 (representative of $\mathcal{C}_{5,6}$)

2.6 Category \mathcal{C}_6

The category \mathcal{C}_6 includes 2250 non-factorizable two-loop Feynman diagrams with seven denominators. According to the topologies of loop structures in \mathcal{C}_6 , we categorize them into 4 subcategories.

The subcategory $\mathcal{C}_{6,1}$ includes 446 two-loop planar double-box diagrams. The topology of their loop structures can be noted as $e12|e3|34|5|e5|e|$ in Nickel index. $\mathcal{C}_{6,1,a}$ includes 424 diagrams and $\mathcal{C}_{6,1,b}$ includes 22 diagrams. $\mathcal{C}_{6,1,a}^{ind}$ has 194 independent diagrams and in $\mathcal{C}_{6,1,b}^{ind}$ has 18 independent diagrams. We choose diagram #23202 as the representative of $\mathcal{C}_{6,1,a}$ and diagram #23228 as the representative of $\mathcal{C}_{6,1,b}$.

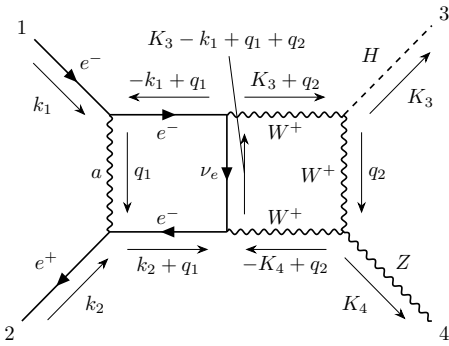


Fig. 26: Diagram #23202 (representative of $\mathcal{C}_{6,1,a}$)

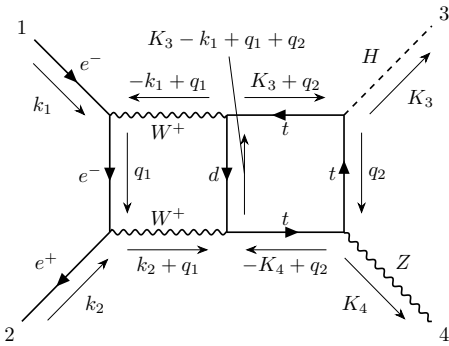


Fig. 27: Diagram #23228 (representative of $\mathcal{C}_{6,1,b}$)

The subcategory $\mathcal{C}_{6,2}$ includes 688 two-loop planar diagrams. The topology of their loop structures can be noted as $e1|22|3|e4|e5|e6|$ in Nickel index. $\mathcal{C}_{6,2,a}$ includes 580 diagrams and $\mathcal{C}_{6,2,b}$ includes 108 diagrams. In $\mathcal{C}_{6,2,b}$, there are 4 diagrams whose amplitudes equal to zero. $\mathcal{C}_{6,2,a}^{ind}$ has 299 independent diagrams and $\mathcal{C}_{6,2,b}^{ind}$ has 48 independent diagrams. We choose diagram #24690 as the representative of $\mathcal{C}_{6,2,a}$ and diagram #24708 as the representative of $\mathcal{C}_{6,2,b}$.

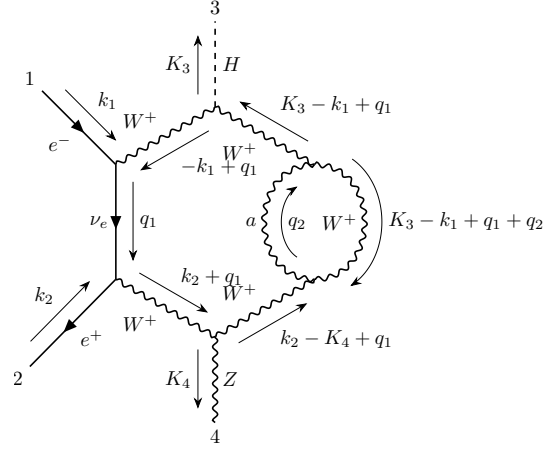


Fig. 28: Diagram #24690 (representative of $\mathcal{C}_{6,2,a}$)

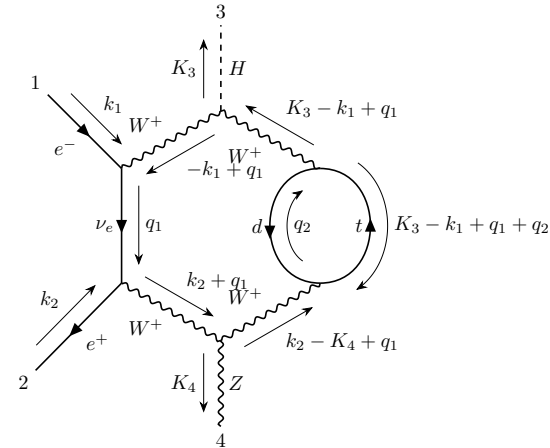


Fig. 29: Diagram #24708 (representative of $\mathcal{C}_{6,2,b}$)

The subcategory $\mathcal{C}_{6,3}$ includes 804 two-loop planar diagrams. The topology of their loop structures can be represented as $e12|e3|e4|45|5|e|$ in Nickel index. $\mathcal{C}_{6,3,a}$ includes 733 diagrams and $\mathcal{C}_{6,3,b}$ includes 71 diagrams. $\mathcal{C}_{6,3,a}^{ind}$ has 302 independent diagrams and $\mathcal{C}_{6,3,b}^{ind}$ has 42 independent diagrams. We choose diagram #23886 as the representative of $\mathcal{C}_{6,3,a}$ and diagram #23907 as the representative of $\mathcal{C}_{6,3,b}$.

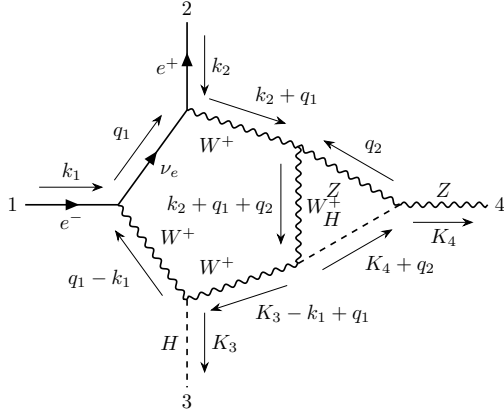


Fig. 30: Diagram #23886 (representative of $\mathcal{C}_{6,3,a}$)

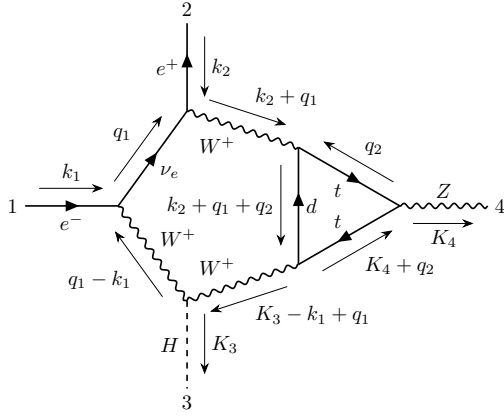


Fig. 31: Diagram #23907 (representative of $\mathcal{C}_{6,3,b}$)

The subcategory $\mathcal{C}_{6,4}$ is the most challenging subcategory which includes 312 two-loop non-planar double-box diagrams. The topology of their loop structures can be noted as $e12|e3|45|45|e|e|$ in Nickel index. $\mathcal{C}_{6,4,a}$ includes

301 diagrams and $\mathcal{C}_{6,4,b}$ includes 11 diagrams. $\mathcal{C}_{6,4,a}^{ind}$ has 146 independent diagrams and $\mathcal{C}_{6,4,b}^{ind}$ has 9 independent diagrams. We choose diagram #22890 as the representative of $\mathcal{C}_{6,4,a}$ and diagram #22909 as the representative of $\mathcal{C}_{6,4,b}$.

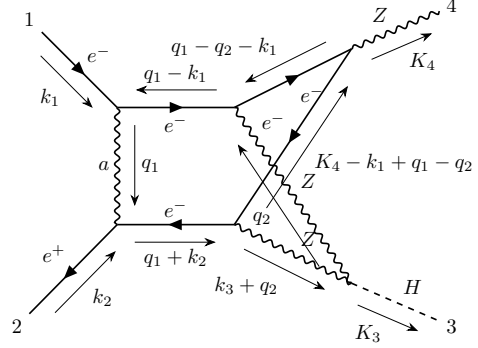


Fig. 32: Diagram #22890 (representative of $\mathcal{C}_{6,4,a}$)

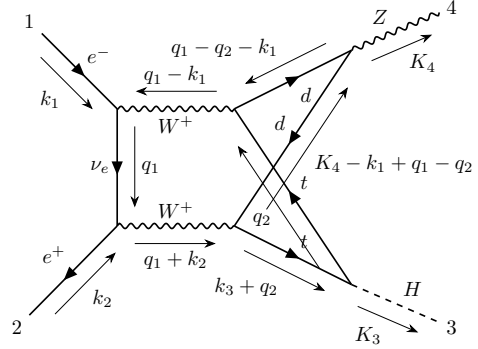


Fig. 33: Diagram #22909 (representative of $\mathcal{C}_{6,4,b}$)

Finally the information for all subcategories has been summarized in Table 1.

Table 1: Summary table for all subcategories

subcategory name	number of diagrams	number of denominators	non-planar diagrams	contains top quark	number of independent diagrams
$C_{1,1}$	2117	-	No	Yes	485
$C_{1,2}$	5513	-	No	Yes	1018
$C_{1,3}$	278	-	No	Yes	82
C_2	18	3	No	No	8
$C_{3,1}$	142	4	No	No	51
$C_{3,2}$	337	4	No	No	93
$C_{3,3}$	114	4	No	No	24
$C_{4,1}$	3266	5	No	Yes	1002
$C_{4,2}$	637	5	No	No	140
$C_{4,3}$	870	5	No	No	278
$C_{5,1}$	4897	6	No	Yes	1436
$C_{5,2}$	184	6	No	No	90
$C_{5,3}$	4067	6	No	Yes	1341
$C_{5,4}$	116	6	No	No	70
$C_{5,5}$	560	6	Yes	Yes	194
$C_{5,6}$	11	6	Yes	No	8
$C_{6,1}$	446	7	No	Yes	212
$C_{6,2}$	688	7	No	Yes	347
$C_{6,3}$	804	7	No	Yes	344
$C_{6,4}$	312	7	Yes	Yes	155

3 Conclusion

In this paper, we categorize the two-loop Feynman diagrams contributing to the $\mathcal{O}(\alpha^2)$ corrections in the Higgsstrahlung $e^+e^- \rightarrow ZH$ into 6 categories and dozens of subcategories. The most challenging subcategory is $C_{6,4}$, which includes 312 two-loop non-planar double-box diagrams. And there are only 155 independent diagrams

in $C_{6,4}$. We hope that the calculations of these Feynman diagrams can be organized conveniently with the help of this categorization.

4 Acknowledgments

The authors want to thank Ayres Freitas, Hao Liang, Tao Liu for helpful discussions.

References

- G. Aad et al., Phys. Lett. B **716**, 1-29 (2012)
- S. Chatrchyan et al., Phys. Lett. B **716**, 30-61 (2012)
- The CEPC Study Group, CEPC Conceptual Design Report: Volume 2 - Physics & Detector, arXiv:1811.10545
- The CEPC Study Group, CEPC Conceptual Design Report: Volume 1 - Accelerator, arXiv:1809.00285
- H. Baer et al., The international linear collider technical design report - volume 2: Physics, arXiv:1306.6352
- T. Behnke et al., The International Linear Collider Technical Design Report - Volume 1: Executive Summary, arXiv:1306.6327
- P. Bambade et al., The International Linear Collider: A Global Project, arXiv:1903.01629
- M. Bicer et al., JHEP, **01**: 164 (2014)
- A. Abada et al., Eur. Phys. J. ST, **228**(2): 261-623 (2019)
- A. Abada et al., Eur. Phys. J. C, **79**(6): 474 (2019)
- B. Ioffe and V. A. Khoze, Sov. J. Part. Nucl., **9**: 50 (1978)
- M. McCullough, Phys. Rev. D, **90**(1): 015001 (2014), [Erratum: Phys.Rev.D 92, 039903 (2015)]
- J. Yan, S. Watanuki, K. Fujii et al., Phys. Rev. D, **94**(11): 113002 (2016)
- F. An et al., Chin Phys C, **43**(4): 043002 (2019)
- ATLAS Collaboration, *Projections for measurements of Higgs boson signal strengths and coupling parameters with the ATLAS detector at a HL-LHC*, ATL-PHYS-PUB-2014-016 (2014), <http://cds.cern.ch/record/1956710>
- Projected performance of an upgraded cms detector at the lhc and hl-lhc: Contribution to the snowmass process, in *Community Summer Study 2013, Snowmass on the Mississippi*, arXiv:1307.7135
- N. Craig, M. Farina, M. McCullough et al., JHEP, **03**: 146 (2015)
- U. Ellwanger, C. Hugonie, and A. M. Teixeira, Phys. Rept., **496**: 1-77 (2010)
- J. Fan, M. Reece, and L.-T. Wang, JHEP, **08**: 152 (2015)
- R. Essig, P. Meade, H. Ramani et al., JHEP, **09**: 085 (2017)
- J. Choi and R. Volkas, Phys. Lett. B, **317**: 385-391 (1993)

-
- 22 J. McDonald, Phys. Lett. B, **323**: 339–346 (1994)
- 23 S. Profumo, M. J. Ramsey-Musolf, and G. Shaughnessy, JHEP, **08**: 010 (2007)
- 24 P. Huang, A. J. Long, and L.-T. Wang, Phys. Rev. D, **94**(7): 075008 (2016)
- 25 J. Fleischer and F. Jegerlehner, Nucl. Phys. B, **216**: 469–492 (1983)
- 26 B. A. Kniehl, Z. Phys. C, **55**: 605–618 (1992)
- 27 A. Denner, J. Kublbeck, R. Mertig et al., Z. Phys. C, **56**: 261–272 (1992)
- 28 Y. Gong, Z. Li, X. Xu et al., Phys. Rev. D, **95**(9): 093003 (2017)
- 29 Q.-F. Sun, F. Feng, Y. Jia et al., Phys. Rev. D, **96**(5): 051301 (2017)
- 30 W. Chen, F. Feng, Y. Jia et al., Chin. Phys. C, **43**(1): 013108 (2019)
- 31 A. Freitas et al., Theoretical uncertainties for electroweak and higgs-boson precision measurements at FCC- ee , arXiv:1906.05379
- 32 Q. Song and A. Freitas., On the evaluation of two-loop electroweak box diagrams for $e^+e^- \rightarrow HZ$ production, arXiv:2101.00308
- 33 P. Nogueira, J. Comput. Phys., **105**: 279–289 (1993)
- 34 T. Hahn, Comput. Phys. Commun., **140**: 418–431 (2001)
- 35 D. Batkovich, Y. Kiriienko, M. Kompaniets et al., GraphState - a tool for graph identification and labelling, arXiv:1409.8227
- 36 B. Nickel, D. Meiron, and G. B. Jr., Compilation of 2-pt and 4-pt graphs for continuous spin model, University of Guelph report
- 37 J. F. Nagle, J.Math.Phys., **7**: 1588–1592 (1966)
- 38 A. I. Davydychev and J. Tausk, Nucl. Phys. B, **397**: 123–142 (1993)